Effat University Repository

Design and evaluation of an analytical model for one-dimensional ballistic Schottky barrier GAA carbon nanotube FETs including BTBT effects

Authors	A. Matter, Fatma;Eslam S., El-Mokadem;F. A Hamed, Hesham;Hussein, Aziza;A. Afifi, Ahmed
Citation	Ibrahim L. Abdalla Fatma A. Matter Eslam S. El-Mokadem Hesham F. A. Hamed Aziza I. Hussein Ahmed. A. Afifi, "Design and evaluation of an analytical model for one-dimensional ballistic Schottky barrier GAA carbon nanotube FETs including BTBT effects. J Comput Electron 24, 115 (2025).
DOI	https://doi.org/10.1007/s10825-025-02337-y
Publisher	Springer Nature
Rights	CC0 1.0 Universal
Download date	2026-05-09 17:47:19
Item License	http://creativecommons.org/publicdomain/zero/1.0/
Link to Item	https://repository.effatuniversity.edu.sa/handle/20.500.14131/2212

Journal of Computational Electronics (2025) 24:115
https://doi.org/10.1007/s10825-025-02337-y

Design and evaluation of an analytical model for one-dimensional ballistic Schottky barrier GAA carbon nanotube FETs including BTBT effects

Ibrahim L. Abdalla[1] · Fatma A. Matter[2] · Eslam S. El-Mokadem[2] · Hesham F. A. Hamed[3,5] · Aziza I. Hussein[4] · Ahmed. A. Afifi[2]

Received: 21 October 2024 / Accepted: 27 April 2025
© The Author(s), under exclusive licence to Springer Science+Business Media, LLC, part of Springer Nature 2025

Abstract
This paper presents a novel analytical model that incorporates the band-to-band tunneling (BTBT) effect for the Schottky-barrier carbon nanotube transistor (SB-CNTFET). This advancement has paved the way for effective routes in designing and simulating ultra-scaled-down circuits. The model has been developed to provide an analytical solution to the current Landauer integral equation. To achieve this solution, approximations for the Fermi–Dirac distribution function, the band-to-band tunneling probability, and the Wentzel-Kramers-Brillouin (WKB) transmission probability have been employed. In this context, the proposed approach was utilized to model a one-dimensional (1D) Schottky barrier (SB) Gate-All-Around (GAA) CNTFET. The suggested model exhibits a high degree of agreement with experimental data, as demonstrated by the following errors: 1.6% in the threshold voltage, 4.5% in the on-current, and 1.35% in the drain-induced barrier lowering (DIBL). Furthermore, the efficiency of the proposed model is underscored by a reported computation time of approximately 1.39 s, representing a significant improvement over existing numerical models. This notable reduction in computing time highlights the advantages of employing an analytical method for CNTFET modeling. Consequently, this work successfully merges the speed and accuracy of circuit simulators.

Keywords Carbon nanotube FET · Analytical model · Band to band tunneling (BTBT) · Ballistic Schottky barrier

1 Introduction

The scaling down of Si-MOSFETs has been the driving force behind technological advancements and circuit evolution. However, this process presents several challenges, such as the short-channel effect and tunneling effects, among others. Unfortunately, the increasing demand for the Internet of Things (IoT), machine learning, artificial intelligence (AI), and internet traffic necessitates the continued scaling down of transistors [1–3]. Carbon nanotube field-effect transistors (CNFETs) are among the most promising candidates to replace Si-MOSFET technology below the 7 nm node [4–7].

This is because they offer high carrier velocity, quasi-ballistic transport, and quasi-one-dimensional (1D) structures.

✉ Ibrahim L. Abdalla
i.l.abdalla@eng.zu.edu.eg

Fatma A. Matter
fatma.mater@hti.edu.eg

Eslam S. El-Mokadem
islam.almokdem@hti.edu.eg

Hesham F. A. Hamed
hfah66@yahoo.com

Aziza I. Hussein
azibrahim@effatuniversity.edu.sa

Ahmed. A. Afifi
ahmed.afifi@hti.edu.eg

1 Department of Electronics and Communications Engineering, Zagazig University, Zagazig 44519, Egypt

2 Department of Electronics and Communication Engineering, Higher Technological Institute, 10th of Ramadan City, Egypt

3 Telecommunication Engineering Department, Egyptian Russian University, Badr City 11829, Egypt

4 Electrical and Computer Engineering Department, Effat University, Jeddah, Kingdom of Saudi Arabia

5 Electrical Engineering Department, Faculty of Engineering, Minia University, Minya, Egypt

Published online: 13 June 2025

Given these characteristics of CNTFETs, the Schottky barrier effect significantly influences device performance. Schottky-barrier (SB) transistors function based on direct tunneling through the SB at the interfaces between the internal channel (intrinsic CNT) and the source (S) and drain (D) metal contacts. Additionally, the dimensional characteristics of the barrier (height and width) are modulated by the application of gate voltage to the device. From a geometrical perspective, the Gate-all-around (GAA), or wrap-gate, structure is considered superior to other CNTFET geometries. This is due to its ability to reduce leakage current and enhance electrical characteristics. Furthermore, this structure shields the nanotube channel from the impact of neighboring devices and stray charges, which can cause variations and instability [8, 9]. This is because they offer high carrier velocity, quasi-ballistic transport, and quasi-one-dimensional (1D) structures. Given these characteristics of CNTFETs, the Schottky barrier effect significantly influences device performance. Schottky-barrier (SB) transistors function based on direct tunneling through the SB at the interfaces between the internal channel (intrinsic CNT) and the source (S) and drain (D) metal contacts. Additionally, the dimensional characteristics of the barrier (height and width) are modulated by the application of gate voltage to the device. From a geometrical perspective, the Gate-all-around (GAA), or wrap-gate, structure is considered superior to other CNTFET geometries. This is due to its ability to reduce leakage current and enhance electrical characteristics. Furthermore, this structure shields the nanotube channel from the impact of neighboring devices and stray charges, which can cause variations and instability.

Numerous efforts have been made to accurately model semiconducting CNTFETs [10–14]. Some studies have utilized the non-equilibrium Green's function (NEGF) formalism, the Wigner transport equation, and the Boltzmann equation to simulate CNTFETs [15–20]. Although these calculation methods yield accurate simulation results, they are unsuitable in terms of memory and computation time. To overcome these challenges, several semi-analytical models have been developed [21–28].

These models significantly improve computation time, but they are still not suitable for application in circuit simulators such as SPICE-like environments. The literature presents various simple analytical models for the drain current of SB-CNTFETs [18, 29–31]. The models mentioned previously are based on an energy-independent transmission probability with a constant effective Schottky barrier (SB) approximation. Unfortunately, these models exclude some important parasitic effects, such as source-to-drain tunneling, band-to-band tunneling (BTBT), and non-ballistic transport, among others.

Such parameters significantly influence the device's behavior and performance metrics, reflecting the unique characteristics of nanoscale transistors. Source-to-drain tunneling is particularly crucial in CNTFET modeling because it directly impacts leakage current and overall power consumption. Accurately modeling this phenomenon is essential for capturing the off-state current and subthreshold behavior, which are critical in short-channel CNTFETs where quantum effects become more pronounced [32, 33].

Band-to-band tunneling (BTBT) is another vital parameter in CNTFET models, playing a decisive role in defining the on-state current and subthreshold swing. Properly accounting for BTBT enables a more accurate representation of the CNTFET's switching characteristics and energy efficiency [34, 35]. Lastly, non-ballistic transport is an essential consideration in CNTFET modeling, particularly due to the one-dimensional nature of carbon nanotubes, where carrier scattering effects are non-negligible. This parameter allows for a more realistic representation of carrier transport mechanisms, especially in devices operating under conditions where the mean free path of carriers is comparable to the device dimensions [36]. In this work, an efficient analytical drain current model for wrap-gate SB-CNTFETs is introduced. Additionally, the proposed model accounts for several influential features, including ballistic transport, transmission through the SB contacts, and band-to-band tunneling.

The novelty of the proposed model:

- It is entirely based on an analytical study, which is reflected in its superior computation time performance.
- It incorporates several influential features, such as ballistic transport and transmission through the Schottky barrier (SB) contacts.
- It includes an explicit formulation of the band-to-band tunneling (BTBT) effect to capture

Precise modeling of BTBT phenomenon is vital for accurately capturing the on-state current and subthreshold behavior, key characteristics in short-channel CNTFETs.

2 Device structure of the GAA CNTFET and physical model

2.1 Device structure

For a comprehensive understanding of the device's structure, this section provides a detailed explanation of its construction. CNTFET devices were fabricated in the ideal wrap-gate geometry with self-aligned gates, successfully scaled down to 20 nm [37].

The stages of achieving a gate-all-around (GAA) structure are illustrated in Fig. 1. As depicted in Fig. 1, the CNTFET is constructed on a silicon-on-insulator (SOI) substrate, with the carbon nanotube (CNT) suspended above it. The gate comprises the suspended CNT, which is coated by a

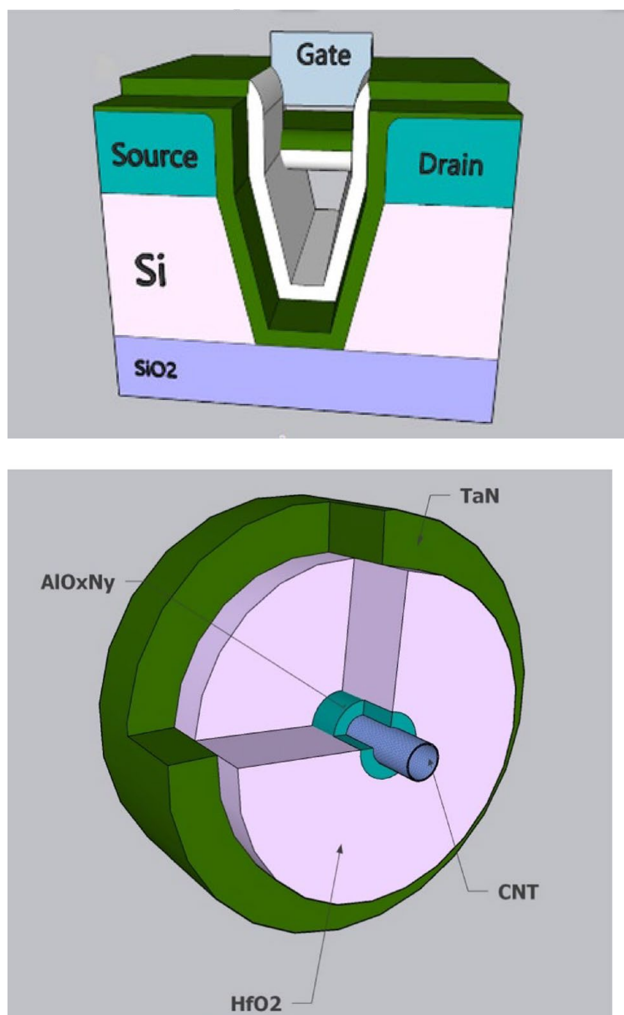

Fig. 1 Gate-all-around (GAA) CNTFET structure

deposited adhesion layer (AlO_xN_y). In addition, two more coating layers are formed, consisting of the gate dielectric (HfO2) and gate metal (TaN), respectively. Furthermore, the source and drain contacts are fabricated from palladium (Pd) material.

The strategic use of multiple dielectrics and coating layers in CNTFET construction is instrumental in addressing various challenges associated with device fabrication and performance optimization. The adhesion layer (AlO_xN_y) is crucial for ensuring that subsequent layers adhere properly to the CNT. It provides a stable foundation for the gate dielectric and gate metal layers, preventing delamination and ensuring structural integrity. The gate dielectric layer (HfO2) is utilized as the gate dielectric due to its high dielectric constant (high-K). This property is essential for achieving high capacitance, which allows for better electrostatic control over the channel. The gate metal layer, made of (TaN), serves as the electrode that controls the channel. It is chosen for its compatibility with (HfO2), providing a stable

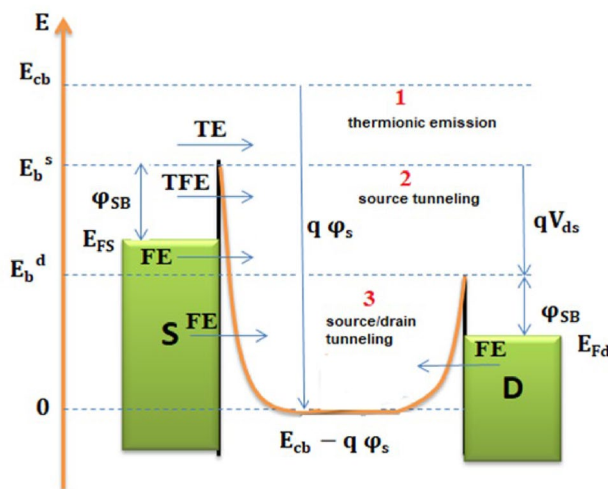

Fig. 2 Energy band diagram of a CNTFET

and reliable electrical contact. (TaN) also aids in maintaining the work function stability required for consistent device operation.

2.2 GAA CNTFET physical insights

Figure 2 illustrates the conduction band profile of the Schottky Barrier Carbon Nanotube Field-Effect Transistor (SB-CNTFET). This diagram describes the various electron injection mechanisms within the device. The energy band is divided into three regions based on the presence of Schottky barriers at the source and drain. Region 1 is characterized by thermionic current, consisting of electrons with sufficient energy to surpass the source potential barrier. As a result, these electrons propagate into the channel from the source without reflection. Region 2 involves electrons from the source with energies below the source potential barrier. These electrons tunnel from the source and move into the channel toward the drain. Notably, they also possess enough energy to overcome the drain potential barrier, allowing them to reach the drain contact without reflection. This process applies in reverse for electrons traveling from the drain to the source. In Region 3, electrons with low energy tunnel from both the source and drain. According to this categorization, three distinct types of currents are associated with electron flow in each of these regions. For Region 1, the primary current is the thermionic emission current (TE). In Region 2, the current includes both the thermionic field emission current (TFE) and the field emission current (FE), representing the flow of electrons through this region. Lastly, the operation of Region 3 is characterized by field emission (FE) tunneling occurring from both the source and the drain.

As illustrated in Fig. 2, ($E_{cb} - q\phi_s$) represents the bottom of the first conduction subband and serves as the model's

energy reference point. Here, ($E_{cb} = E_g/2$), where (E_g) is the energy band gap and (φ_S) denotes the surface potential. (L) signifies the total length of the channel, which is also considered the gate length (L_g). ($E_{Fs(d)}$) indicates the Fermi levels of the source and drain relative to the energy reference point

$$E_{FS(d)} = q\varphi_S - E_{cb} - qV_{s(d)} \tag{1}$$

$$E_b^{S(d)} = \varphi_{SB} + q\varphi_S - E_{cb} - qV_{s(d)} \tag{2}$$

where (φ_{SB}) represents the Schottky barrier height, referenced to ($E_{Fs(d)}$), the Fermi levels of the source and drain. It is calculated as ($\varphi_{SB} = \varphi_M - \chi_{sc}$), where ($\varphi_M$) is the metal work function and (χ_{sc}) is the electron affinity. ($E_b^{S(d)}$) denotes the potential barrier height at the source and drain with respect to the reference point.

The energy band model is based on Evanescent-mode analysis [38–40] and is used to derive the band edge profile. The channel electrostatic potential, denoted by ($\varphi(r)$) in cylindrical coordinates, is composed of two components. The first component is the longitudinal channel potential ($\varphi_l(r)$), obtained by solving the Laplace equation along the transport direction. The second component is the transverse channel potential ($\varphi_t(r)$), derived from solving Poisson's equation and equated to (φ_S). Additionally, the conduction sub-band edges at the source side, ($E_L^c(Z)$), and the drain side, ($E_R^c(Z)$), at any point along the channel are represented by exponential functions [41].

$$E_L^c(Z) = E_{cb} - q\varphi_S + E_b^S \exp\left(-\frac{Z}{\lambda}\right) \tag{3}$$

$$E_R^c(Z) = E_{cb} - q\varphi_S + E_b^d \exp\left(\frac{Z-L}{\lambda}\right) \tag{4}$$

Here, (λ) is a characteristic length representing the decay of the electrostatic potential, which can be interpreted as an effective Schottky barrier (SB) width. The value of (λ) is determined by (5), provided that the diameter of the Carbon Nanotube (CNT), (d_{CNT}), is smaller than the oxide thickness (t_{ox}), as is the case in Gate-All-Around CNTFETs [42].

$$\lambda = \frac{2t_{ox} + d_{CNT}}{2.405} \tag{5}$$

2.3 CNTFET current equation

The electron current in a CNTFET is determined using the Landauer–Büttiker integral [43]. This formula involves integrating, with respect to energy, the product of three probability types, as shown in (6):

$$I_e = \frac{4q}{h}\int_0^{\infty} T_{tunn}(E)\left[f_{FD}\left(E - E_{FS}\right) - f_{FD}\left(E - E_{Fd}\right)\right]dE \tag{6}$$

Here, ($T_{tunn}(E)$) is the total transmission probability, accounting for band-to-band tunneling:

$$T_{tunn}(E) = T_{SB}^S(E)T_{SB}^d(E)T_{BTBT}(E) \tag{7}$$

The first factor, the Fermi–Dirac distribution function $f_{FD}\left(E - E_{Fs(d)}\right)$, represents the occupation probability for electrons in the source and drain contacts, as shown in (8) [44]:

$$f_{FD}\left(E - E_{Fs(d)}\right) = \frac{1}{\left\{exp\left[\frac{(E-E_{Fs(d)})}{K_BT}\right] + 1\right\}} \tag{8}$$

where (K_B) is the Boltzmann constant and (T) is temperature. The second probability, ($T_{SB}^{S(d)}(E)$), specifies electron tunneling through the Schottky barrier (SB) at the source and drain, respectively.

This probability is crucial in determining the tunneling current through the device and is influenced by factors such as the energy of the electrons, the potential barrier height at the interfaces, and the effective mass of the charge carriers. The transmission probability is determined using the Wentzel-Kramers-Brillouin (WKB) approximation method [41] as shown in (9) and (10).

where $\left(\alpha = \frac{4\lambda\sqrt{m^*}}{\hbar}\right)$ with electron effective mass $\left(m^* = \frac{8E_{cb}\hbar^2}{3a^2V_\pi^2}\right)$, where (a = 2.49 Å) is the carbon–carbon atom distance, and $V_\pi \approx 3.033eV$ is the $\pi - \pi$ π − π π − π π − π π − π bond energy in the tight binding model [43].

$$T_{SB}^{S(d)}(E) = \begin{cases} 1 & E_b^{S(d)} < E \\ \exp\left(-\alpha\sqrt{E_b^{S(d)}}\gamma\left(E/E_b^{S(d)}\right)\right) & 0 < E < E_b^{S(d)} \end{cases} \tag{9}$$

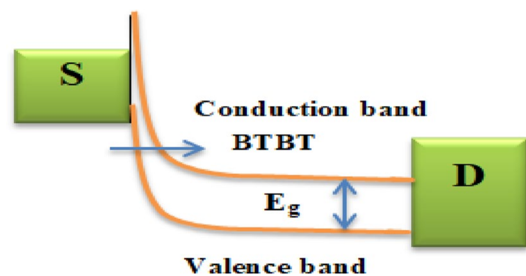

Fig. 3 BTBT phenomenon

$$\gamma_{SB}(x) = \sqrt{1-x} - \sqrt{x}tan^{-1}\left(\sqrt{\frac{1-x}{x}}\right), x = \frac{E}{E_b^{S(d)}} \quad (10)$$

Lastly, Band-to-Band Tunneling ($T_{BTBT}(E)$) represents the probability of electrons tunneling from the valence band to the conduction band through the band gap, and vice versa. This phenomenon occurs when the sub-band energy ($E_b^{s(d)}$) exceeds the band gap energy (E_g). Figure 3 illustrates this phenomenon.

For the parabolic one-band approximation method, the band-to-band tunneling (BTBT) probability, ($T_{BTBT}(E)$), can be expressed by (11) and (12). Here, (E_{cb}) represents the energy at the bottom of the first conduction subband of the carbon nanotube (CNT) when the gate voltage is zero.

Finally, the total transmission probability can be expressed as in (13).

$$T_{tunn}(E) = \begin{cases} 1 & E_b^{S(d)} < E \\ T_{SB} & E_b^{S(d)} - E_g < E < E_b^S \\ T_{BTBT} & 0 < E < E_b^{S(d)} - E_g \\ 0 & E < 0 \end{cases} \quad (11)$$

$$T_{BTBT}^{S(d)}(E) = \begin{cases} 1 & E_b^{S(d)} < E \\ \exp\left(-\alpha\sqrt{2E_{cb}}\gamma\left(E/2E_{cb}\right)\right) & 0 < E < E_b^{S(d)} \end{cases} \quad (12)$$

$$\gamma_{BTBT}(x) = 1 - \sqrt{x}tan^{-1}\left(\sqrt{\frac{1}{x}}\right), x = \frac{E}{2E_{cb}} \quad (13)$$

3 Mathematical model

3.1 Mathematical model strategy

The primary goal of mathematical modeling is to solve the Landauer–Büttiker integral analytically. This is achieved by making appropriate approximations for both the occupation and transmission probabilities. While addressing this problem, several key observations must be considered. First, the functions ($\gamma_{SB}(x)$) and ($\gamma_{BTBT}(x)$) can be represented as polynomials of ($\sqrt{x}$). Given the existence of their derivatives with respect to ($\sqrt{x}$) as ($\sqrt{x}$)→0, the corresponding polynomial representation ($P_n\left(\sqrt{x}\right)$) can be expressed as shown in (14).

$$P_n\left(\sqrt{x}\right) = a_1\sqrt{x} + \sum_{i=0}^{\infty} a_{2i}\left(\sqrt{x}\right)^{2i} \quad (14)$$

Regarding to the fact that x ranges from 0 to 1, it is sufficient to taking the polynomial orders into concern up to the third order. As a result of this, $P_n\left(\sqrt{x}\right)$ can be formulated as follows in (15).

Given that (x) ranges from 0 to 1, it is sufficient to consider polynomial orders up to the third order. Consequently, ($P_n\left(\sqrt{x}\right)$) can be formulated as shown in (15).

$$P_n\left(\sqrt{x}\right) = a_0 + a_1\sqrt{x} + a_2 x \quad (15)$$

On the other hand, ($f_{FD}\left(E - E_F\right)$) is a decreasing probability distribution function that varies asymptotically at its bounds. Additionally,

($f_{FD}\left(E - E_F\right)$) reaches its maximum at the point $(-\infty, 1)$ and has an inflection point at$(0, 0.5)$. This allows for a piecewise representation of ($f_{FD}\left(E - E_F\right)$), as shown in (16).

$$f_{FD}\left(E - E_F\right) = \begin{cases} 1 - 0.5\exp\left[b_1\left(\frac{E-E_F}{K_BT}\right)\right] & E < E_F \\ 0.5exp\left[-b_1\left(\frac{E-E_F}{K_BT}\right)\right] & \text{otherwise} \end{cases} \quad (16)$$

It is important to note that the same positive value (b_1) is used for both categories of piecewise approximation to maintain equality and ensure integration continuity at ($E = E_F$). Moreover, for very large values of (E), ($f_{FD}\left(E - E_F\right)$) tends to:

$$f_{FD}\left(E - E_F\right) = \exp\left(\frac{E_F - E}{K_BT}\right) \quad (17)$$

To properly account for the asymptotic behavior of ($f_{FD}\left(E - E_F\right)$), its piecewise representation must be modified as shown in (18)

$$f_{FD(\text{app})}\left(E - E_F\right) = \begin{cases} 1 - 0.5\exp\left[b_1\left(\frac{E-E_F}{K_BT}\right)\right] & E < E_F \\ 0.5\exp\left[-b_1\left(\frac{E-E_F}{K_BT}\right)\right] & E_F \le E \le E_F + b_2K_BT \\ \exp\left(\frac{E_F-E}{K_BT}\right) & \text{otherwise} \end{cases} \quad (18)$$

To ensure the continuity of the piecewise representation, the value (b_2) is determined as shown in (19).

$$b_2 = \frac{\ln 2}{1 - b_1} \quad (19)$$

Here, ($b_1 = 0.7213$). Based on the previous observations, the Landauer–Büttiker integrands can be expressed in the form of a Gaussian distribution in terms of ($\sqrt{E}$). Consequently, the Landauer–Büttiker integration can be interpreted as the computation of an error function (*erf*) in terms of ($\sqrt{E}$). The remaining step is to transform the Landauer–Büttiker

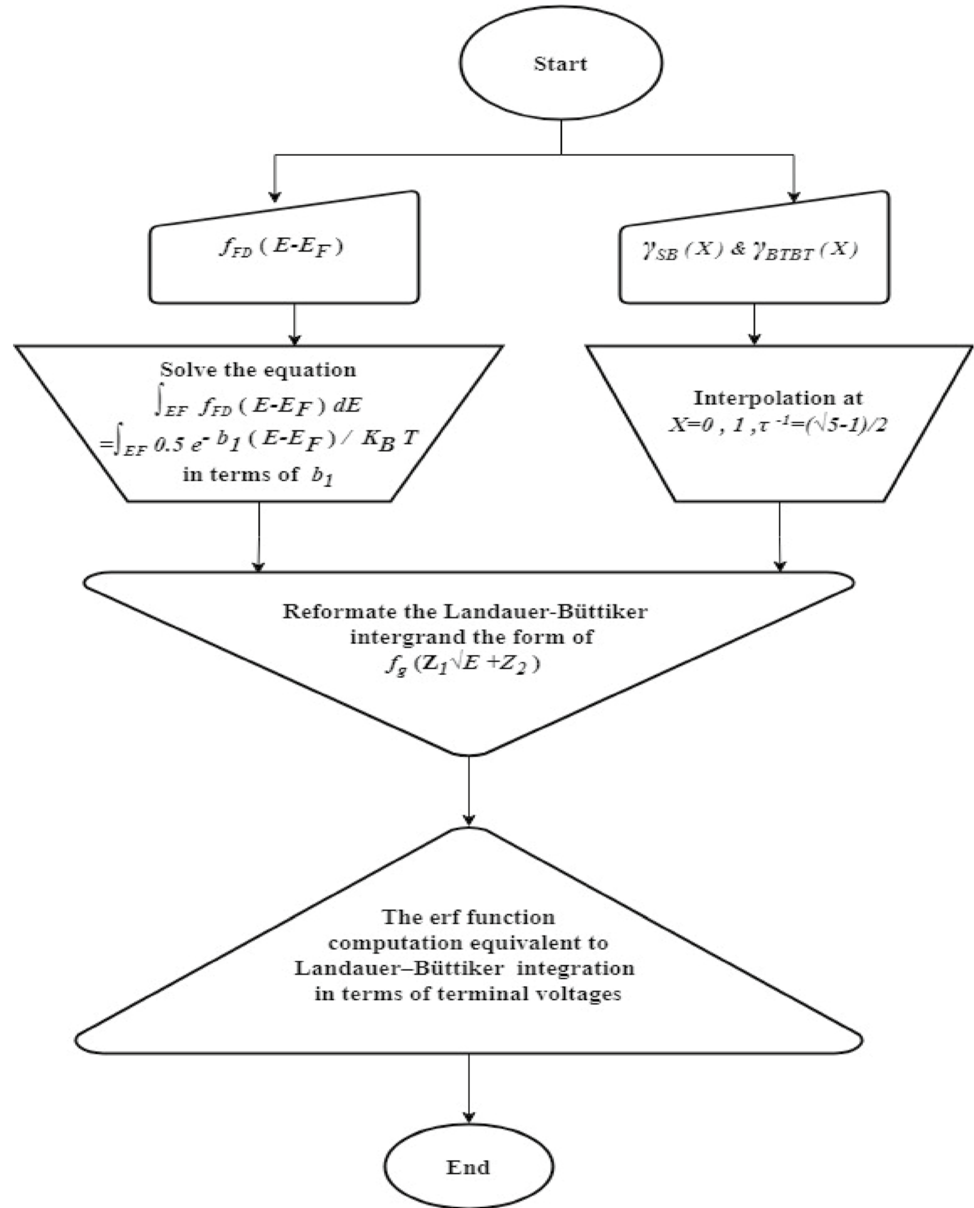

Fig. 4 Flowchart of the Mathematical model

integration into an *(erf)* formula. This is achieved by extracting the values ofa_0,a_1, and a_2 for both $\gamma_{SB}(x)$ and $\gamma_{BTBT}(x)$, as well as the exponent (b_1) for ($f_{FD}\left(E-E_F\right)$) illustrated in flowchart of Fig. 4. Referring to the flowchart in Fig. 4, Eq. (15) can represent any polynomial of any order for the values ($x = 0, 1, \text{and} \tau^{-1} = \frac{\sqrt{5}-1}{2}$), where ($\tau = \frac{1+\sqrt{5}}{2}$) is the golden ratio. Therefore, it is advantageous to interpolate ($\gamma_{SB}(x)$) and ($\gamma_{BTBT}(x)$) at these values to determine the coefficients in Eq. (15). On the other hand, the first and last segments of the piecewise representation of ($f_{FD}\left(E-E_F\right)$) align well with the original function in terms of both equality and continuity. The middle segment compensates for any discrepancies by adjusting the value of its exponent so that the area under its curve matches that of the original function for ($E \geq E_F$). Additionally, the value (b_1) is used in the definitions of the first and last segments, as mentioned earlier, to ensure the best fit of the middle segment curve to the original function.

3.2 Approximated transmission probability $T_{SB(app)}(E)$ and BTBT probability $T_{BTBT(app)}(E)$

3.2.1 Approximated Schottky barrier tunneling probability $\mathbf{T_{SB(app)}(E)}$

Based on the mathematical model described in the previous section, the approximated value of ($\gamma_{SB}(x)$) is given by:

$$\gamma_{SB(app)}(x) = Px - (P+1)\sqrt{x} + 1 \tag{20}$$

where $P = \frac{\left(\tau\gamma(1/\tau)-\tau+\sqrt{\tau}\right)}{\left(1-\sqrt{\tau}\right)} \approx 0.7113.$

The absolute error of $\gamma_{SB(app)}(x)$ in (20) is less than 0.02 for all ($x \in [0,1]$). Consequently, the approximated Schottky Barrier Tunneling Probability $T_{SB(app)}(E)$ can be expressed as shown in (21)

$$T^{S(d)}_{SB(app)} = exp\left(-\alpha\sqrt{E^{S(d)}_b}\gamma_{SB(app)}\left(E/E^{S(d)}_b\right)\right) \tag{21}$$

For Region 1 ($E > E^S_b$):E > $E_b{}^s$ E > $E_b{}^s$ Thermally excited electrons propagate into the channel without tunneling, so ($T^{S(d)}_{SB} = 1$)$T_{SB}{}^{s(d)} = 1$ $T_{SB}{}^{s(d)} = 1$ $T_{SB}{}^{s(d)} = 1$ $T_{SB}{}^{s(d)} = 1$.**For Region 2** ($E^d_b < E < E^S_b$):$E_b{}^d$ < E < $E_b{}^s$ $E_b{}^d$ < E < $E_b{}^s E_b{}^d$ < E < $E_b{}^s E_b{}^d$ < E < $E_b{}^s$Electrons tunnel only through the Schottky barrier (SB) at the source. Therefore, ($T^S_{SB} = T^S_{SB(app)}$) as represented by (22), and ($T^d_{SB} = 1$).

For Region 3 ($E < E^d_b$):E < $E_b{}^d$ E < $E_b{}^d$ Electrons tunnel through both Schottky barriers located at the source and drain.Thus ($T_{SB(app)} = T_{SB(app)2b}$) as represented by (23). In this region, we neglect the multiple reflections of electrons between the two potential barriers, as they represent a second-order contribution to the net current.

3.2.2 Approximated BAND TO BAND Tunneling probability $T_{BTBT(app)}(E)$

Similarly, the approximated value of ($\gamma_{BTBT}(x)$) will be denoted by (22).Consequently, ($T_{BTBT(app)}(E)$) will be expressed as shown in (25)

$$\gamma_{BTBT}(x) = Qx - \left(Q + \frac{\pi}{4}\right)\sqrt{x} + 1 \tag{22}$$

where $Q = \pi + \sqrt{\tau}\left(1 + \frac{\pi/4}{\sqrt{\tau}-1}\right) - P.$

The absolute error of ($\gamma_{BTBT(app)}(x)$) in (24) is less than 0.03 for all ($x \in [0,1]$).

3.3 Total current

As shown in Fig. 5, the current from the source and drain can be classified into three components: thermionic emission current (TE), thermionic field emission current (TFE), and field emission current (FE).

$$T^S_{SB(app)} = exp\left(-\alpha\sqrt{E^S_b}\left(P\frac{E}{E^S_b} - (P+1)\sqrt{\frac{E}{E^S_b}} + 1\right)\right) = exp\left(-A_1E + B_1\sqrt{E} - C_1\right) \tag{23}$$

where

$$A_1 = \frac{\alpha P}{\sqrt{E^S_b}}, B_1 = \alpha(P+1), C_1 = \alpha\sqrt{E^S_b}$$

$$A_1 = \frac{\alpha p}{\sqrt{E^s_b}}B_1 = \alpha(p+1)C_1 = \alpha\sqrt{E^s_b}$$

$$T_{SB(app)} = T_{SB(app)2b} = T^S_{SB(app)} \times T^d_{SB(app)} = exp\left(-A_2E + B_2\sqrt{E} - C_2\right) \tag{24}$$

where

$$A_2 = \alpha P\left(\frac{1}{\sqrt{E^S_b}} + \frac{1}{\sqrt{E^d_b}}\right), B_2 = 2\alpha(P+1), C_2 = \alpha\left(\sqrt{E^S_b} + \sqrt{E^d_b}\right)$$

$$T_{BTBT(app)}(E) = exp\left(-\alpha\sqrt{2E_{cb}}\left(Q\frac{E}{2E_{cb}} - \left(Q + \frac{\pi}{4}\right)\sqrt{\frac{E}{2E_{cb}}} + 1\right)\right) = exp\left(-A_{BTBT}E + B_{BTBT}\sqrt{E} - C_{BTBT}\right) \tag{25}$$

where $A_{BTBT} = \frac{\alpha Q}{\sqrt{2E_{cb}}}, B_{BTBT} = \alpha\left(Q + \frac{\pi}{4}\right), C_{BTBT} = \alpha\sqrt{2E_{cb}}$

.

Thermionic emission (TE) current occurs in region 1 when the energy level is greater than the Schottky barrier (SB) height at both the source and the drain, i.e., ($E > E^{S(d)}_b$). In this scenario, the transmission probability is considered to be 1, and we utilize the original expression for the Fermi–Dirac distribution function ($f_{FD}(E - E_F)$) as stated in (8).

$$I^{s(d)}_{TE} = \frac{4q}{h}K_BTln\left(1 + exp\left(-\frac{E^{S(d)}_{TE}}{K_BT}\right)\right) \tag{26}$$

where $E^{S(d)}_{TE} = \varphi_{SB} + qV_{s(d)}$.

For the calculation of thermionic field emission (TFE) and field emission (FE) currents, we utilize the approximations for both the Fermi–Dirac distribution function ($f_{FD(app)}(E - E_F)$) and the transmission.

probability $T_{(app)}$, as detailed in Appendix 1. TFE current occurs in regions 2 and 3, at energy levels between those of TE and FE currents, specifically where ($E > E_{Fs(d)}$). The FE current, on the other hand, arises from electrons tunneling below the Fermi level, where ($E < E_{Fs(d)}$).

For small gate-source voltages (V_{gs}) and large drain-source voltages (V_{ds}), specifically when$\left(q\varphi_S \le E_{cb} - \varphi_{SB} + qV_{ds}\right)$, there exists only one Schottky barrier (SB) located at the

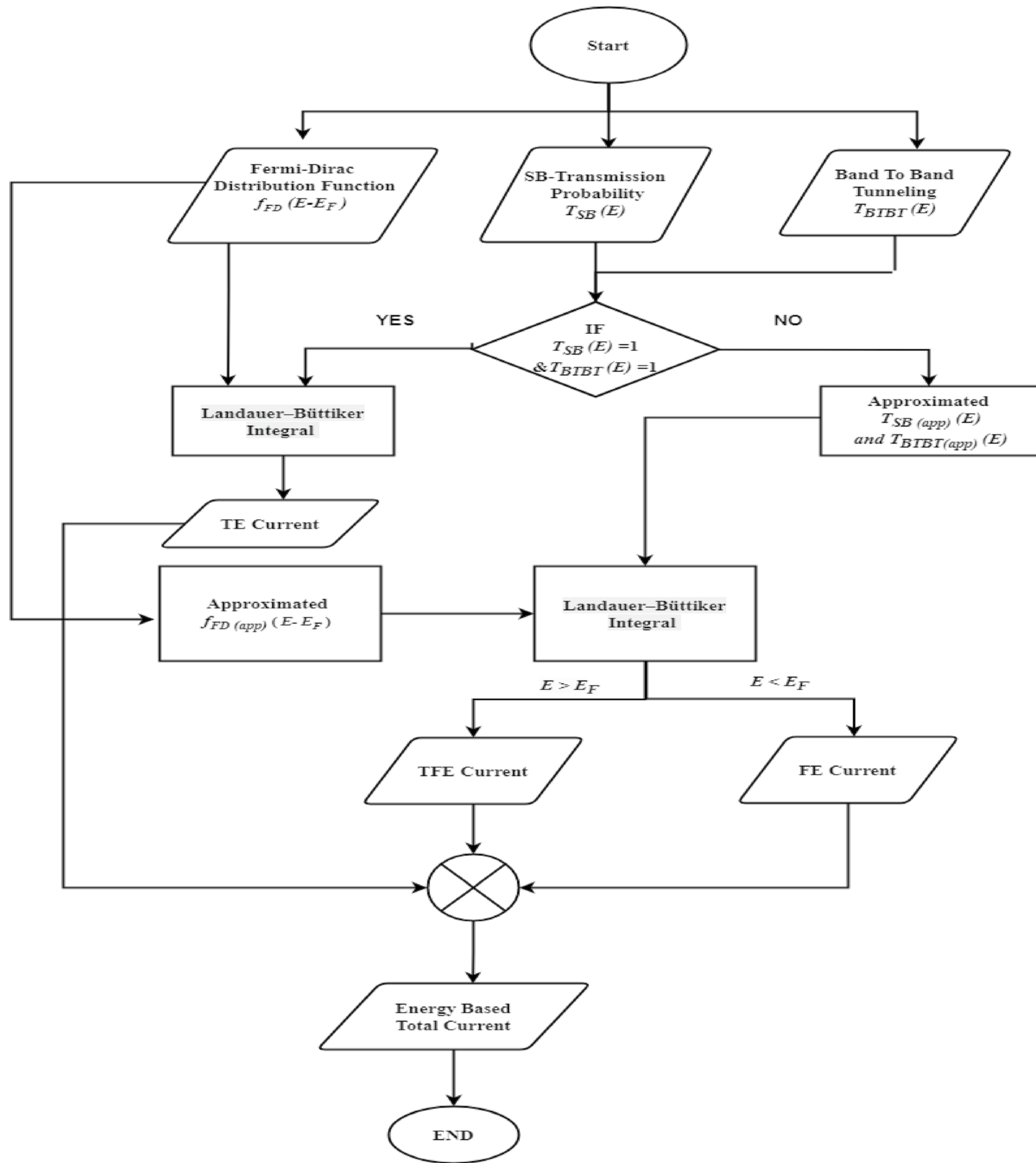

Fig. 5 Flowchart of computing total electron current

source, where ($E_b^S > 0$) and ($E_b^d < 0$). The source and drain currents will be as follows:

$$I^S = \begin{cases} I_{FE}^S(0, E_{FS}) + I_{TFE}^S(E_{FS}, E_b^S) + I_{TE}^S, E_{FS} \geq 0 \\ I_{TFE}^S(0, E_b^S) + I_{TE}^S, E_{FS} < 0 \end{cases} \quad (27)$$

$$I^d = I_{TFE}^d(0, E_b^S) + I_{TE}^d \quad (28)$$

For large gate-source voltages (V_{gs}) and small drain-source voltages (V_{ds}), specifically when $(q\varphi_S \geq E_{cb} - \varphi_{SB} + qV_{ds})$, there are two Schottky barriers (SB) present, one at the source and another at the drain, with ($0 < E_b^d < E_b^S$). The source and drain currents will be represented by Eqs. (29) and (30), respectively.

Table 1 Model parameters

Symbol	Description	Value
V_{gs}, V_{ds}	Gate, drain to source voltage	Bias dependent
E_g	Energy gap	0.647 eV
E_{cb}	Bottom of the first conduction subband	0.3235 eV
L_g	Gate length	30 nm
φ_{SB}	Schottky barrier height	Fitting parameter
$E_{Fs(d)}$	The source and drain Fermi level	Bias dependent
a	Carbon–carbon atom distance	2.45 AO
V_π	$\pi - \pi$ bond energy	≈ 3.033 eV
λ	Characteristic length	Fitting parameter
φ_S	Surface potential	Bias dependent
d_{CNT}	CNT diameter	1.33 nm
t_{ox}	Gate insulator thickness	8 nm

$$I^s = \begin{cases} I^S_{TFE}\left(0, E^d_b\right) + I^S_{TFE}\left(E^d_b, E^S_b\right) + I^S_{TE}, & E_{FS} < 0 \\ I^S_{FE}\left(0, E_{FS}\right) + I^S_{TFE}\left(E_{FS}, E^d_b\right) + I^S_{TFE}\left(E^d_b, E^S_b\right) + I^S_{TE}, & 0 < E_{FS} < E^d_b \\ I^S_{FE}\left(0, E^d_b\right) + I^S_{FE}\left(E^d_b, E_{FS}\right) + I^S_{TFE}\left(E_{FS}, E^S_b\right) + I^S_{TE}, & E_{FS} > E^d_b \end{cases} \tag{29}$$

$$I^d = \begin{cases} {}^d_{TFE}\left(0, E^d_b\right) + I^d_{TFE}\left(E^d_b, E^S_b\right) + I^d_{TE}, & IE_{Fd} < 0 \\ I^d_{FE}\left(0, E_{Fd}\right) + I^d_{TFE}\left(E_{Fd}, E^d_b\right) + I^d_{TFE}\left(E^d_b, E^S_b\right) + I^d_{TE}, & E_{Fd} > 0 \end{cases} \tag{30}$$

The total current can be expressed as follows:

$$I_T\left(V_{gs}, V_{ds}\right) = I^S\left(V_{gs}, V_{ds}\right) - I^d\left(V_{gs}, V_{ds}\right) \tag{31}$$

4 Results

We compare the simulation results from our proposed model with the available experimental data in [37]. The parameters used in the simulation for our proposed model are listed in Table 1.

The simulation model's transfer and output characteristics have been graphically represented to closely align with the experimental results. This alignment was achieved through the empirical adjustment of the parameters described above, ensuring a precise match.

4.1 Fitting process

The fitting process in our model involves adjusting the Schottky barrier height (φ_{SB}) and the characteristic length (λ) to align the simulation results with experimental data. The Schottky barrier height (φ_{SB}) determines how easily electrons can flow between the metal contacts and the nanotube channel. A lower barrier height facilitates higher current flow. Additionally, variations in (φ_{SB}) influence the operating voltage range of the transistor. Consequently, this parameter is used to match the saturation current levels in the transfer characteristics and the threshold voltage (V_{th}).

The characteristic length (λ) represents the decay of the electrostatic potential from the gate into the channel region. For shorter channel lengths, (λ) becomes increasingly significant as it affects the device's susceptibility to short-channel effects, such as drain-induced barrier lowering (DIBL). A larger (λ) relative to the channel length can exacerbate these effects. Based on empirical data, (λ) is used to horizontally adjust the logarithmic transfer characteristics, ensuring they align with the DIBL effects observed in experimental results.

4.2 Results and discussion

During the attempt to simultaneously match the transfer and output characteristics, it was noted that the experimental data from [37] showed inconsistencies between the two curves. Specifically, the drain current (I_{ds}) did not correspond for the same gate voltage (V_{gs}) and drain voltage (V_{ds}) across both sets of measurements. For example, at ($V_{gs} = 0.75V$) V and ($V_{ds} = 0.3V$) V, the (I_{ds}) was recorded as approximately 2.47 µA in the transfer characteristics, but 6.689 µA in the output characteristics. This mismatch is believed to stem from possible differences in the experimental setups used to collect data for each curve, as well as variations in the fabrication process affecting device parameters. Due to the

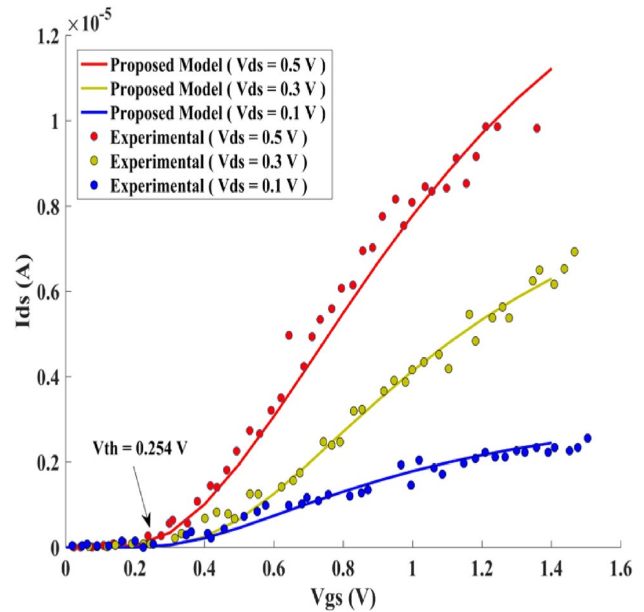

Fig. 6 Comparison of linear transfer characteristics i.e., I_{ds} versus V_{gs} for various drain bias voltages V_{ds} between experimental data [37] and simulated results

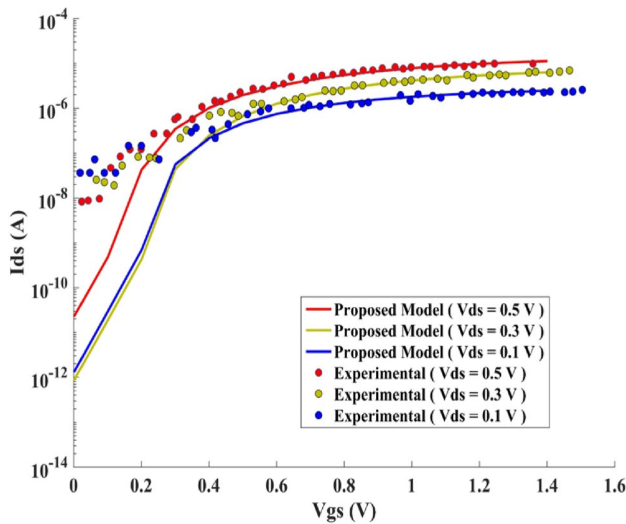

Fig. 7 Comparison of log-linear transfer characteristics i.e., I_{ds} versus V_{gs} for various drain bias voltages V_{ds} between experimental data [37] and simulated results

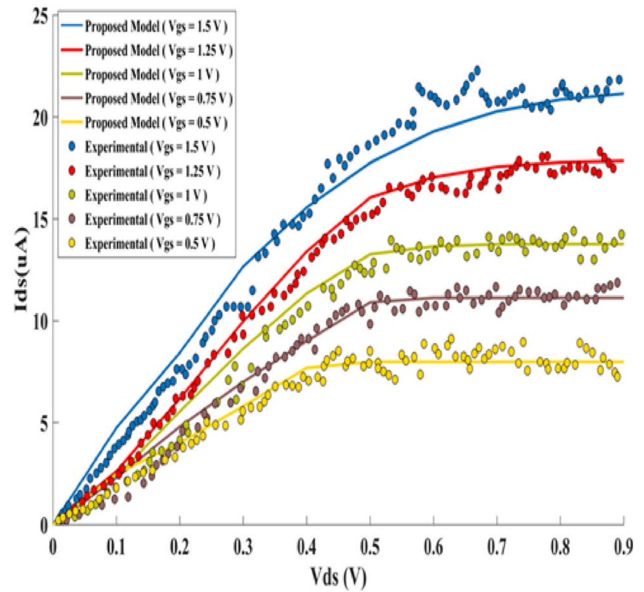

Fig. 8 Shows the simulated output characteristic i.e., I_{ds} versus V_{ds} with varying V_{gs}, plotted against the corresponding experimental results

substantial variation observed, it was not possible to achieve a satisfactory fit for both curves simultaneously. As a result, each curve was fitted separately.

Figure 6 shows the simulated transfer characteristics, i.e., I_{ds} versus V_{gs} at varying V_{ds}, plotted against the corresponding experimental results. For clarity, Fig. 6 is also plotted in a semi-log scale, as shown in Fig. 7. The plots demonstrate good agreement between the analytical results from the proposed model and the experimental data in the ON-state of the device (above the threshold voltage).

However, a closer examination of Fig. 7 reveals that the experimental results in the subthreshold regions deviate by approximately one order of magnitude. This is because a short-channel device exhibits numerous additional second-order effects, such as source-to-drain tunneling, which play a significant role in the subthreshold region. Our model does not account for multiple reflections between the Schottky barriers located at the source and drain. Consequently, further mathematical refinement is needed in the future to accurately align both curves when viewed from a semi-log perspective. This presents an opportunity to enhance our model by adjusting or adding to an existing analytical model to better predict the subthreshold characteristics.

From Fig. 6, we can extract the threshold voltage (V_{th}) by fitting a line to the high slope segment of the curve and extrapolating it to the x-axis. Moreover, we can determine the drain induced barrier lowering (DIBL), an essential parameter that refers to the reduction in the threshold voltage of the transistor at higher drain voltages. It is defined as the ratio of the change in threshold voltage (V_{th}) to the change in drain-source voltage (V_{ds}) [31] The fitting values used for obtaining these characteristics are: $\varphi_{SB} = 0.3235eV$ and $= 5nm$.

Figure 8 illustrates the simulated output characteristic of the device, specifically I_{ds} versus V_{ds} for varying V_{gs}. The plots in the figure showcase closely matching saturation currents, with the correlation improving as (V_{gs}) increases. However, in the linear region where ($V_{ds} < V_{gs} - V_{th}$), the trends in the experimental data do not align accurately, particularly for ($V_{gs} < 0.75$ V). Yet, it presents values that are quite close to the real measurements, with a deviation of no more than $\pm 17\%$. Despite the discrepancies in the linear region, the model demonstrates accurate saturation currents. This suggests that the model can be effectively utilized to predict device performance with reasonable error, particularly in regions where the trends match experimental data closely. Further refinements may be necessary to enhance the model's accuracy in predicting behaviors in the linear region, especially for lower gate-source voltages.

Table 2 Comparison of device characteristic between model simulation results and experimental data

Metric	Proposed model	Experimental data
Threshold voltage V_{th} (V)	0.254	0.25
Drain induced barrier lowering DIBL ((mV/V)	≈150	≈148
On current I_{on} (μA) I_{on} I_{on} (μA) (μA)	11.06	11.58

Table 3 Computation time Comparison

Model	Proposed model	Ref [45]	Ref [46]
Computation time (s)	1.39	20.65	86.23

Various established measures of device performance have been recorded, depending on their availability, in order to numerically evaluate the comparison between experimental data and simulation results, as outlined in Table 2.

According to Table 2, the simulated results closely match the experimental values on the threshold voltage with an error of about 1.6%, the on-current with an error of 4.5%, and the drain-induced barrier lowering (DIBL) with an error of 1.35%.

In summary, the proposed analytical model demonstrates strong validation for ON-state performance and offers reasonable accuracy in capturing the essential characteristics of the modeled device across all operational regions. However, further mathematical refinement is needed in the future to enhance the model's accuracy in the subthreshold region.

4.3 Computation time comparison

We compared computational time of our proposed model with two existing numerical models [45, 46] that simulate a CNTFET structure (GAA CNTFET) similar to the one used in [37]. The comparison results are presented in Table 3.

Notably, the computation time for the proposed model is approximately 1.39 s, demonstrating its efficiency compared to the existing numerical models. Although the actual runtimes may vary depending on the system and application, the data clearly show that the proposed analytical model offers superior computational efficiency. This significant reduction in computation time can be attributed to the analytical nature of the model, which avoids the need for computationally intensive numerical integrations.

5 Conclusions

This study proposes a novel analytical model for one-dimensional gate-all-around (GAA) Schottky barrier carbon nanotube field-effect transistors (SB-CNTFETs), incorporating band-to-band tunneling phenomena. The model is founded on straightforward, hand-calculated approximations. Our analytical approach focuses on deriving clear, hand-calculated, and accurate approximations for the band-to-band tunneling probability, Schottky Barrier tunneling transmission probability, and the Fermi–Dirac Distribution Function**.** This methodology significantly simplifies the calculations involved in the current equation.

Additionally, the proposed model demonstrates exceptional accuracy when compared with experimental measurements across various parameters: on-current, with an error margin of 4.5%; drain-induced barrier lowering (DIBL), with an error of 1.35%; and threshold voltage, with an error of 1.6%. Moreover, our fully analytical model achieves a superior computation time of approximately 1.39 s.

Future research could build upon this innovative framework to further refine sub-threshold operation. Potential enhancements include integrating multiple reflections between the Schottky barriers (SBs) at the source and drain into our model and considering electron source-to-drain tunneling. Another avenue for improvement involves replacing the single carbon nanotube (CNT) with multi-CNT configurations to enhance transport efficiency.

Appendix 1

Derivation of TFE and FE current Equations.

TFE current equations

Case 1: if $x > A + \frac{1}{b_1 K_B T}$

$$I_{TFE}(E_1, E_2) = \frac{q \exp\left(\frac{E_F}{b_1 K_B T} + C\Delta\right)}{hx} \left[B\sqrt{\frac{\pi}{x}} \exp\left(-C + \frac{B^2}{4x}\right) \left(erfc\left(\sqrt{xE_2} - \frac{B}{2\sqrt{X}}\right) - erfc\left(\sqrt{xE_1} - \frac{B}{2\sqrt{X}}\right)\right) + 2\left(\exp\left(-xE_2 + B\sqrt{E_2} - C\right) - \exp\left(-xE_1 + B\sqrt{E_1} - C\right)\right)\right.$$

Case 2: if $x = A + \frac{1}{b_1 K_B T}$

$$I_{TFE}(E_1, E_2) = \frac{8q\exp\left(\frac{E_F}{b_1 K_B T} + C\Delta\right)}{2hB^2}\left[\begin{array}{c}\exp\left(B\sqrt{E_2} - C\right)\left(1 - B\sqrt{E_2}\right)\\ -\left(\exp\left(B\sqrt{E_1} - C\right)\left(1 - B\sqrt{E_1}\right)\right)\end{array}\right]$$

Case 3: if $x < A + \frac{1}{b_1 K_B T}$

$$I_{TFE}(E_1, E_2) = \frac{4q\exp\left(\frac{E_F}{b_1 K_B T} + C\Delta\right)}{h|x|}\left[\begin{array}{l}\frac{B}{2}\sqrt{\frac{\pi}{|x|}}\left(\exp\left(-xE_2 - |x|E_2 - \left(C + \frac{B^2}{4|x|}\right)\right)erfi\left(\sqrt{|x|E_2} + \frac{B}{2\sqrt{|x|}}\right) - \exp\left(-xE_1 - |x|E_1 - \left(C + \frac{B^2}{4|x|}\right)\right)erfi\left(\sqrt{|x|E_1} + \frac{B}{2\sqrt{|x|}}\right)\right)\\ -\left(\exp\left(-xE_2 + B\sqrt{E_2} - C\right) - \exp\left(-xE_1 + B\sqrt{E_1} - C\right)\right)\end{array}\right]$$

FE current equations

Case 1: if $x > A - \frac{1}{b_1 K_B T}$

$$\begin{aligned} I_{FE}(E_1, E_2) = &\frac{2q\exp(C\Delta)}{ha}\left[B\exp\left(\frac{B^2}{4A} - C\right)\left(erfc\left(\sqrt{AE_2} - \frac{B}{2\sqrt{A}}\right) - erfc\left(\sqrt{AE_1} - \frac{B}{2\sqrt{A}}\right)\right)\right.\\ &\left.+2\left(\exp\left(-AE_2 + B\sqrt{E_2} - C\right) - \exp\left(-AE_1 + B\sqrt{E_1} - C\right)\right)\right]\\ &-\frac{q}{ha}\exp\left(C\Delta - \frac{E_{FS(d)}}{b_1 K_B T}\right)\\ &\left[B\sqrt{\frac{\pi}{x}}\exp\left(\frac{B^2}{4x} - C\right)erfc\left(\sqrt{xE_2} - \frac{B}{2\sqrt{X}}\right)\left(-erfc\left(\sqrt{xE_1} - \frac{B}{2\sqrt{X}}\right)\right)\right.\\ &\left.+2\left(\exp\left(-xE_2 + B\sqrt{E_2} - C\right) - \exp\left(-xE_1 + B\sqrt{E_1} - C\right)\right)\right] \end{aligned}$$

Case 2: if $x = A - \frac{1}{b_1 K_B T}$

$$I_{FE}(E_1, E_2) = \frac{2q\exp(C\Delta)}{ha}\left[\begin{array}{c}\left(1 - B\sqrt{E_2}\right)\left(\exp\left(\frac{-E_2}{b_1 K_B T} + B\sqrt{E_2} - C\right) - \frac{1}{2}exp\left(\frac{-E_{FS(d)}}{b_1 K_B T} + B\sqrt{E_2} - C\right)\right)\\ -\left(1 - B\sqrt{E_1}\right)\left(\exp\left(\frac{-E_1}{b_1 K_B T} + B\sqrt{E_1} - C\right) - \frac{1}{2}exp\left(\frac{-E_{FS(d)}}{b_1 K_B T} + B\sqrt{E_1} - C\right)\right)\end{array}\right]$$

Case 3: if $x < A - \frac{1}{b_1 K_B T}$

$$
\begin{aligned}
I_{TFE}(E_1,E_2) = {} & \frac{2q\exp(C\Delta)}{h|A|}\left[B\sqrt{\frac{\pi}{|x|}}\left(\exp\left(-AE_2-|A|E_2-\left(C+\frac{B^2}{4|A|}\right)\right)erfi\left(\sqrt{|A|E_2}+\frac{B}{2\sqrt{|A|}}\right)\right.\right.\\
& \left.\left.-\exp\left(-AE_1-|A|E_1-\left(C+\frac{B^2}{4|A|}\right)\right)\left(erfi\left(\sqrt{|A|E_1}+\frac{B}{2\sqrt{|A|}}\right)\right)\right)\right]\\
& \left[B\sqrt{\frac{\pi}{|x|}}\left(\exp\left(-AE_2-|A|E_2-\left(C+\frac{B^2}{4|A|}\right)\right)erfi\left(\sqrt{|A|E_2}+\frac{B}{2\sqrt{|A|}}\right)e-\exp\left(-AE_1-|A|E_1-\left(C+\frac{B^2}{4|A|}\right)\right)erfi\left(\sqrt{|A|E_1}+\frac{B}{2\sqrt{|A|}}\right)\right)\right.\\
& \left.-2\left(\exp\left(-AE_2+B\sqrt{E_2}-C\right)-\exp\left(-AE_1+B\sqrt{E_1}-C\right)\right)\right]\\
& -\frac{q\exp\left(C\Delta-\frac{E_F}{b_1K_BT}\right)}{h|x|}\\
& \left[B\sqrt{\frac{\pi}{|x|}\left(\exp\left(-xE_2-|x|E_2-\left(C+\frac{B^2}{4|x|}\right)\right)erfi\left(\sqrt{|x|E_2}+\frac{B}{2\sqrt{|x|}}\right)-\exp\left(-xE_1-|x|E_1-\left(C+\frac{B^2}{4|x|}\right)\right)erfi\left(\sqrt{|x|E_1}+\frac{B}{2\sqrt{|x|}}\right)\right)}\right.\\
& \left.+2\left(\exp\left(-xE_2+B\sqrt{E_2}-C\right)-\exp\left(-xE_1+B\sqrt{E_1}-C\right)\right)\right]
\end{aligned}
$$

Author contributions Fatma A. Matter: design and simulation results Ibrahim L. Abdalla, Ahmed. A. Afifi, Eslam S. El-Mokadem: wrote the main manuscript text Aziza I. Hussein, Hesham F. A. Hamed: Final revision of the manuscript.

Funding The authors have not disclosed any funding.

Data availability No datasets were generated or analyzed during the current study.

Declarations

Competing interests The authors declare no competing interests.

References

1. Barla, P., Joshi, V.K., Bhat, S.J.J.O.C.E.: Spintronic devices: a promising alternative to CMOS devices. J. Comput. Electron. **20**(2), 805–837 (2021)
2. El-Mokadem, E.S., et al.: Design and performance evaluation of vehicular visible light communication system under different weather conditions and system parameters. Opto-Electron. Rev. **31**, 145580–145580 (2023)
3. EL-Mokadem, E.S., et al.: Throughput enhancement of cognitive M2M networks based on NOMA for 5G communication systems. Int. J. Commun. Syst. **33**(12), 4468 (2020)
4. Darwin, S., et al. *Performance Analysis of Carbon Nanotube Transistors-A Review*. In: *2022 6th International Conference on Trends in Electronics and Informatics (ICOEI)*. 2022. IEEE.
5. Sharma, A., A. Kumar, and S.C. Sharma. *Effect of Process Parameters on CNTFET*. in *Advances in Manufacturing Technology and Management: Proceedings of 6th International Conference on Advanced Production and Industrial Engineering (ICAPIE)—2021*. 2022. Springer.
6. Kavitha, S., et al.: Design and implementation of CNFET SRAM cells by using multi-threshold technique. Electronics **12**(7), 1611 (2023)
7. Ding, H., Chen, L., Huang, W.J.I.E.E.: Designing high-speed and energy-efficient dynamic comparators using complementary carbon nanotube field-effect transistors. IEICE Electron Express **20**(19), 20230373–20230373 (2023)
8. Patel, P., et al. *CNTFET: Comparative Study of Planar and Coaxial*. In: *2022 IEEE International Conference on Nanoelectronics, Nanophotonics, Nanomaterials, Nanobioscience & Nanotechnology (5NANO)*. 2022. IEEE.
9. Bozorgmehr, A., et al.: A high-performance fully programmable membership function generator based on 10 nm gate-all-around CNTFETs. AEU-Int. J. Electron. Commun. **123**, 153293 (2020)
10. Guo, J., Lundstrom, M., Datta, S.: Performance projections for ballistic carbon nanotube field-effect transistors. Appl. Phys. Lett. **80**(17), 3192–3194 (2002)
11. Dwyer, C., M. Cheung, and D.J. Sorin. Semi-empirical SPICE models for carbon nanotube FET logic. In: 4th IEEE Conference on Nanotechnology, 2004. 2004. IEEE.
12. Raychowdhury, A., Mukhopadhyay, S., Roy, K.: A circuit-compatible model of ballistic carbon nanotube field-effect transistors. IEEE Trans. Comput. Aided Des. Integr. Circuits Syst. **23**(10), 1411–1420 (2004)
13. Natori, K., Kimura, Y., Shimizu, T.: Characteristics of a carbon nanotube field-effect transistor analyzed as a ballistic nanowire field-effect transistor. J. Appl. Phys. **97**(3), 034306 (2005)
14. Neophytou, N., Guo, J., Lundstrom, M.S.: Three-dimensional electrostatic effects of carbon nanotube transistors. IEEE Trans. Nanotechnol. **5**(4), 385–392 (2006)
15. Guo, J., Datta, S., Lundstrom, M.: A numerical study of scaling issues for Schottky-barrier carbon nanotube transistors. IEEE Trans. Electron Devices **51**(2), 172–177 (2004)

16. Leonard, F., Stewart, D.A.: Properties of short channel ballistic carbon nanotube transistors with ohmic contacts. Nanotechnology **17**(18), 4699 (2006)
17. Ossaimee, M., et al.: Ballistic transport in Schottky barrier carbon nanotube FETs. Electron. Lett. **44**(5), 336–337 (2008)
18. Maneux, C., et al.: Multiscale simulation of carbon nanotube transistors. Solid-State Electron. **89**, 26–67 (2013)
19. Anjum, N., et al. *Numerical Analysis to Determine the Temperature-Dependent Charge Transport in CNTFET*. In: *2021 IEEE International Women in Engineering (WIE) Conference on Electrical and Computer Engineering (WIECON-ECE)*. 2021. IEEE.
20. Sarbazi, H., Sabbaghi-Nadooshan, R., Hassanzadeh, A.J.I.J.O.E.: Process validation test of CNTFET using Stanford model. Int. J. Electron. **109**(1), 1–22 (2022)
21. Jiménez, D., et al.: A simple drain current model for Schottky-barrier carbon nanotube field effect transistors. Nanotechnology **18**(2), 025201 (2006)
22. Vega, R.A.: On the modeling and design of Schottky field-effect transistors. IEEE Trans. Electron Devices **53**(4), 866–874 (2006)
23. Vega, R.A.: Comparison study of tunneling models for Schottky field effect transistors and the effect of Schottky barrier lowering. IEEE Trans. Electron Devices **53**(7), 1593–1600 (2006)
24. Hazeghi, A., Krishnamohan, T., Wong, H.-S.P.: Schottky-barrier carbon nanotube field-effect transistor modeling. IEEE Trans. Electron Devices **54**(3), 439–445 (2007)
25. Sinha, S., Balijepalli, A., Cao, Y.: Compact model of carbon nanotube transistor and interconnect. IEEE Trans. Electron Devices **56**(10), 2232–2242 (2009)
26. Michetti, P., Iannaccone, G.: Analytical model of one-dimensional carbon-based Schottky-barrier transistors. IEEE Trans. Electron Devices **57**(7), 1616–1625 (2010)
27. Tripathy, S., Bhattacharyya, T.K.J.S.-S.E.: Semi analytical model for electrical transport in single wall carbon nanotube thin film transistors. Solid-State Electron. **180**, 107988 (2021)
28. Marani, R., Perri, A.G.J.I.J.O.N.: Nanotechnology, *analysis and design of CNTFET-based electronic circuits: a review*. Int. J. Nanosci. Nanotechnol. **19**(3), 149–164 (2023)
29. Deng, J., Wong, H.-S.P.: A compact SPICE model for carbon-nanotube field-effect transistors including nonidealities and its application—Part I: model of the intrinsic channel region. IEEE Trans. Electron Devices **54**(12), 3186–3194 (2007)
30. Kazmierski, T.J., et al.: Numerically efficient modeling of CNT transistors with ballistic and nonballistic effects for circuit simulation. IEEE Trans. Nanotechnol. **9**(1), 99–107 (2009)
31. Najari, M., et al.: Schottky barrier carbon nanotube transistor: compact modeling, scaling study, and circuit design applications. IEEE Trans. Electron Devices **58**(1), 195–205 (2010)
32. Gooran-Shoorakchaly, A., Sharif, S.S., Banad, Y.M.J.J.O.C.E.: A simulation study of electrostatically doped silicene and graphene nanoribbon FETs. J. Comput. Electron. **23**(6), 1315–1324 (2024)
33. Tamersit, K., et al.: Performance projection of vacuum gate dielectric doping-free carbon nanoribbon/nanotube field-effect transistors for radiation-immune nanoelectronics. Nanomaterials **14**(11), 962 (2024)
34. Kumaran, V.S., et al.: Modeling and simulation of quantum state distribution in graphene nanoribbon GaN/InSb TFETs for high-precision biosensing applications. Sensing Imag. **26**(1), 4 (2024)
35. Raj, B., Raman, A.: Nanoscale Semiconductors. CRC Press, Boca Raton (2022)
36. Zahoor, F., et al.: Carbon nanotube field effect transistors: an overview of device structure, modeling, fabrication and applications. Phys. Scr. **98**(8), 082003 (2023)
37. Franklin, A.D., et al.: Carbon nanotube complementary wrap-gate transistors. Nano Lett. **13**(6), 2490–2495 (2013)
38. Frank, D.J., Taur, Y., Wong, H.-S.: Generalized scale length for two-dimensional effects in MOSFETs. IEEE Electron Device Lett. **19**(10), 385–387 (1998)
39. Monroe, D. and J. Hergenrother. *Evanescent-mode analysis of short-channel effects in fully depleted SOI and related MOSFETs*. In: *1998 IEEE International SOI Conference Proceedings (Cat No. 98CH36199)*. 1998. IEEE.
40. Oh, S.-H., Monroe, D., Hergenrother, J.M.: Analytic description of short-channel effects in fully-depleted double-gate and cylindrical, surrounding-gate MOSFETs. IEEE Electron Device Lett. **21**(9), 445–447 (2000)
41. Bejenari, I., Schröter, M., Claus, M.: Analytical drain current model of 1-D ballistic Schottky-barrier transistors. IEEE Trans. Electron Devices **64**(9), 3904–3911 (2017)
42. Lee, C.-S., et al.: A compact virtual-source model for carbon nanotube FETs in the sub-10-nm regime—Part I: intrinsic elements. IEEE Trans. Electron Devices **62**(9), 3061–3069 (2015)
43. Wong, H.-S.P., Akinwande, D.: Carbon nanotube and graphene device physics. Cambridge University Press (2011)
44. Kheiri, G., *Analysis of Current Variation Through a Field Effect Transistor Based on Asymmetric Zigzag Carbon Nanotubes.* 2022.
45. Koswatta, S., J. Guo, and D. Nikonov, *MOSCNT: code for carbon nanotube transistor simulation*. 2006.
46. Budiman, G.W., et al., *Cylindrical CNT MOSFET Simulator*. 2014.

Publisher's Note Springer Nature remains neutral with regard to jurisdictional claims in published maps and institutional affiliations.

Springer Nature or its licensor (e.g. a society or other partner) holds exclusive rights to this article under a publishing agreement with the author(s) or other rightsholder(s); author self-archiving of the accepted manuscript version of this article is solely governed by the terms of such publishing agreement and applicable law.